Synergistic Impact of Passivation and Efficient Hole Extraction on Phase Segregation in Mixed Halide Perovskites

*Zhaojie Zhang, Rebecca J. Gilchrist, Miu Tsuji, Ronald L. Grimm, Tomoyasu Mani, D. Venkataraman**

Data Availability

The data underlying this study is openly available in Scholarworks@UMassAmherst at DOI (Will be provided after acceptance).

Conflict of Interest

The authors declare no conflict of interest.

Author Emails and ORCID

D. Venkataraman:
dv@umass.edu
0000-0003-2906-0579

Zhaojie Zhang
zhaojiezhang@umass.edu
0000-0001-9259-4720

Rebecca J. Gilchrist (RJG):
rgilchrist@wpi.edu
0009-0005-2218-6373

Ronald L. Grimm (RLG):
grimm@wpi.edu
0000-0003-0407-937X

Tomoyasu Mani
tomoyasu.mani@uconn.edu
0000-0002-4125-5195

Miu Tsuji:
miu.tsuji@uconn.edu
0009-0001-7634-9343

Synergistic Impact of Passivation and Efficient Hole Extraction on Phase Segregation in Mixed Halide Perovskites

*Zhaojie Zhang, Rebecca J. Gilchrist, Miu Tsuji, Ronald L. Grimm, Tomoyasu Mani, D. Venkataraman**

Zhaojie Zhang, D. Venkataraman
Department of Chemistry, University of Massachusetts Amherst, Amherst, MA 01003, United States
E-mail: dv@umass.edu

Rebecca J. Gilchrist, Ronald L. Grimm
Department of Chemistry and Biochemistry, WPI Life Sciences and Bioengineering Center, Worcester Polytechnic Institute, Worcester, MA 01609, United States

Miu Tsuji, Tomoyasu Mani
Department of Chemistry, University of Connecticut, Storrs, CT 06269, United States

Keywords: phase segregation, perovskites, hole transport layers, charge carriers

The interface between the hole transport layer (HTL) and perovskite in p-i-n perovskite solar cells (PSCs) plays a vital role in the device performance and stability. However, the impact of this interface on the vertical phase segregation of mixed halide perovskite remains insufficiently understood. In this work, we systematically investigate the impact of chemical and electronic properties of HTL on vertical halide segregation of mixed-halide perovskites. We show that incorporating a PTAA/CuI_xBr_{1-x} bilayer as the HTL significantly suppresses light-induced vertical phase segregation in $MAPb(I_{0.7}Br_{0.3})_3$. We used grazing-incidence X-ray diffraction (GIXRD) to capture the depth-resolved composition change of $MAPb(I_{0.7}Br_{0.3})_3$ at the interface and within the bulk under illumination. By changing the illumination direction and the electronic properties of HTL, we elucidated the roles of charge carrier extraction and interfacial defects on vertical phase segregation. The PTAA/CuI_xBr_{1-x} bilayer, with its synergistic passivation and efficient hole extraction ability, stabilizes the interface and bulk of the mixed halide perovskite layer and prevents phase segregation. This work underscores that synergetic

passivation and efficient hole extraction pack a more powerful punch for arresting the vertical phase segregation in mixed-halide perovskite.

1. Introduction

An attractive feature of mixed halide perovskites is that their bandgaps can be predictably varied by changing the halide ratios.[1] Thus, their optoelectronic properties can be matched for maximal performance for applications such as solar cells or light-emitting diodes (LEDs). Indeed, many of the perovskite-based solar cells with high power conversion efficiencies use mixed halide perovskites as active materials.[2,3] However, the essential device inputs for device operation—light in solar cells and injected charge in LEDs—trigger the halide ions to migrate and segregate into domains.[1,4–6] This process initiates the irreversible degradation of the perovskites, reduces the effective bandgap, and diminishes the performance of the devices.[7] The valence band offsets between segregated domains localize holes in iodide-rich domains, exacerbate the oxidation of iodide ions, and destabilize the crystal lattice.[8–11] Therefore, the halide migration in mixed halide perovskites needs to be arrested to ensure long-term device stability and maintain their high performance.

What causes the halides to migrate in mixed halide perovskites? Initial studies pointed to local electric fields generated by trapped photogenerated charge carriers as the driving force for halide migration away from illuminated regions.[12] The light direction-dependent phase segregation was attributed to the different migration rates between iodides and bromides under the photogenerated electric fields[13] or carrier gradients[14]. Subsequent studies correlated halide migration to strain induced by photo-generated polarons.[5,15] These models emphasized the impact of defect-assisted ion migration and photogenerated charge carriers on halide segregation and highlighted the complex interactions at play.[14,16] Recent studies point to the accumulation of trapped charges especially trapped holes as a key factor.[16,17] However, extracting the charges from the active layer by the hole transport layer alone does not seem to arrest the halide migration. For example, a study by Herz and co-workers found that coating a poly(triarylamine) (PTAA) on a mixed halide perovskite can mitigate the halide migration in the bulk but still led to halide segregation at the hole-transport layer (HTL)/perovskite interface.[18] A lingering question is—what is the nature of the HTL that will lead to stable mixed halide devices?

We answer this question herein by studying copper halide-based hole transport bilayers. We had reported the use of CuBr as an HTL for inverted perovskite solar cells.[19] We had also reported a PTAA/CuI hole transport bilayer for inverted perovskite solar cells that exhibited a high PCE of >20% and notable operation stability.[20] By adjusting the halide ratio in CuI_xBr_{1-}

$_x$, we can alter the electronic properties including energy levels, hole density, mobility, and conductivity.[21] Copper halides can also passivate the defects at the perovskite/HTL interface via halogen bonding.[22] Thus, copper halides provide a great platform to study the impact of HTL, including electronic properties and defects passivation capabilities, on the photostability of mixed-halide perovskites. We fabricated devices using $MAPb(I_{0.7}Br_{0.3})_3$ as the active layer and PTAA and PTAA/CuI_xBr_{1-x} as hole transport layers in the inverted solar cell device configuration. The devices were fabricated on glass and on indium tin oxide (ITO). We mapped the composition change on the surface and the bulk using grazing incidence powder X-ray diffraction (GIXRD), measured the emission lifetimes and charge extraction efficiencies using time-resolved photoluminescence spectroscopy (TRPL), studied the passivation effects by calculating the Urbach energies using UV-vis absorption spectroscopy, and determined the changes to the frontier energy levels using ultraviolet photoelectron spectroscopy (UPS). The samples were illuminated either from the ITO/glass side or the top of the device to probe the influence of the light direction on halide migration. Based on our studies, we show that to arrest the halide migration, holes need to be moved away from the perovskite/HTL interface and that a single layer of HTL may be insufficient. Our results also show that a hole transport bilayer on ITO arrests halide migration compared to the bilayer on glass indicating that any accumulation of charge in the hole transport layer can facilitate ion migration. Additionally, we found that the use of copper halides passivates the defects at the perovskite/HTL interface, but passivation alone is insufficient to arrest halide migration. Transferring the extracted holes away from to perovskite/HTL interface to the ITO electrode, together with the passivation of the interface, is necessary for arresting the halide segregation. Our studies provide a viable pathway to fabricate stable devices with mixed halide perovskites as active layers.

2. Results and Discussions

To study the impact of HTL and substrate types on the vertical phase segregation of mixed halide perovskites, $MAPb(I_{0.7}Br_{0.3})_3$ (hereafter referred to as MAPbIBr) was deposited on bare substrates (ITO-coated glass or glass), and on substrates coated with hole transport layers PTAA or PTAA/CuI_xBr_{1-x}. For copper halides, we used CuI, $CuI_{0.5}Br_{0.5}$, or CuBr. CuI exhibits higher conductivity (10^2 $S \cdot cm^{-1}$), hole density (10^{19} cm^{-3}), and hole mobility (1 cm^2 V^{-1} s^{-1}) than CuBr (10^{-2} $S \cdot cm^{-1}$, 10^{17} cm^{-3}, 10^{-1} cm^2 V^{-1} s^{-1}, respectively) and these parameters vary predictably with halide composition.[21] Thus $CuI_{0.5}Br_{0.5}$ serves as a midpoint for these parameters. For substrates, we chose a conducting (ITO-coated glass) and an insulating (glass) substrate. A

PMMA layer was deposited on top of the MAPbIBr layer to eliminate the effect of moisture and ambient air (see Experimental Section).[18]

We used GIXRD to probe the chemical composition of MAPbIBr at various depths. The penetration depths of grazing incident X-ray for perovskite were estimated to be ~70, 150, and 500 nm for incident angles (ω) of 0.5°, 1°, and 3°, respectively.[23] The thickness of the MAPbIBr film was measured by a profilometer to be ~400 nm. Thus, the diffraction data from low incident angles contains structural information of the sample at or near the surface. At ω=3°, the X-ray diffraction data includes bulk structural information. The GIXRD patterns of MAPbIBr films exhibit dominant characteristic peaks at 14.4°, 20.3°, and 28.8° which are assigned to (100), (110) and (200) planes of MAPbIBr, respectively, as previously reported.[1]

We exposed encapsulated MAPbIBr films on different HTL and substrates to white LED light (100 mW cm^{-2}) for 4 h in ambient air. The MAPbIBr films were illuminated either from the top (PMMA side) or from the bottom (glass/ITO side) to investigate how illumination direction affects ion migration. After 4 hours of illumination aging, the MAPbIBr films were taken out immediately for GIXRD studies. The data collection for the GIXRD experiment takes about 15 min whereas the remixing of halides under dark takes hours.[24] Thus, the GIXRD data does capture the composition changes that occur in the film upon illumination. The composition changes of MAPbIBr films were captured by monitoring the (100) peak of GIXRD patterns before and after illumination. The pristine MAPbIBr deposited on different HTL, and substrates have similar GIXRD patterns, indicating that the MAPbIBr grown on different HTL, and substrates have consistent crystal composition and orientation.

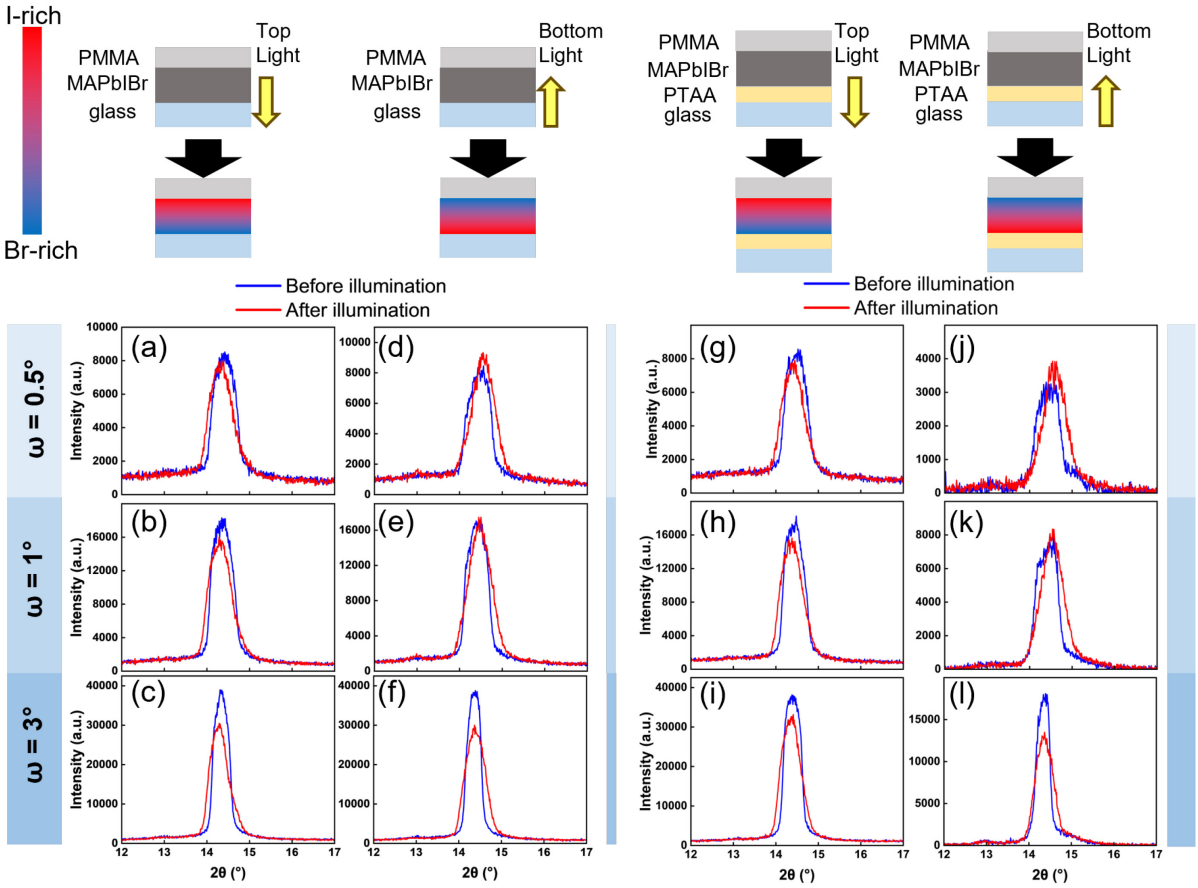

Figure 1. GIXRD patterns of (100) peak of glass/MAPbIBr and glass/PTAA/MAPbIBr with ω=0.5°, 1° and 3° before (blue) and after illumination (red). Schematic representations of sample architectures and light-induced vertical composition changes are attached to the top of each column of GIXRD patterns. When the samples are illuminated from the top, the (100) peak with ω=0.5° for both (a) glass/MAPbIBr and (g) glass/PTAA/MAPbIBr shift to lower diffraction angles, indicating the appearance of I^--rich domains at the top surface. Peak broadening is observed for both (b, c) glass/MAPbIBr and (h, i) glass/PTAA/MAPbIBr with ω=1° and 3°, indicating the appearance of Br^--rich domains at the bottom interface. When the samples are illuminated from the bottom, the (100) peak with ω=0.5° for both (d) glass/MAPbIBr and (j) glass/PTAA/MAPbIBr shift to higher diffraction angles, indicating the appearance of Br^--rich domains at the top surface. Peak broadening is observed for both (e, f) glass/MAPbIBr and (k, l) glass/PTAA/MAPbIBr with ω=1° and 3°, indicating the appearance of I^--rich domains at the bottom interface.

When we illuminated the glass/MAPbIBr films from the top (i.e., the light enters from the MAPbIBr/PMMA interface, as illustrated in **Figure 1**), in the GIXRD pattern with ω=0.5°, we observed that the (100) peak shifted to a lower 2θ, indicating that the top surface has become I^-

-rich. When we increased ω to 1°, we observed the growth of both high and low 2θ components and thus a broadened (100) peak. We also observed peak broadening and a decrease in peak intensity when the incident X-ray angle was ω=3°. Both peak broadening and decrease in peak intensity are characteristics of phase segregation in mixed halide perovskites with Br^- content less than 0.5.[25] The coexistent low and high diffraction angle components in the GIXRD pattern at ω=1° and 3° support the coexistence of I^--rich and Br^--rich domains. Considering that the I^--rich domains appear at the top interface (MAPbIBr/PMMA interface), we surmise that the bottom interface (glass/MAPbIBr interface) is Br^--rich.

When we illuminated the glass/MAPbIBr films from the bottom, at ω=0.5°, we observed that the (100) diffraction peak shifted to higher 2θ, indicating that the top surface has become Br^--rich. We also observed peak broadening when ω=1° and 3° indicating the formation of I^--rich domains at the bottom interface. From GIXRD observations, we conclude that the illumination leads to vertical phase segregation, and the direction of vertical halide migration depends on the direction of the incident light. The interface closer to the incident light becomes I^--rich while the farther interface becomes Br^--rich. This observation is consistent with a prior report that concluded that iodides tend to migrate toward the light source.[26]

We then deposited PCBM on glass/MAPbIBr films and monitored their phase stability by GIXRD (See **Figure S1**). For the glass/MAPbIBr/PCBM samples, no PMMA layer was deposited on top as the encapsulation layer because the PCBM could be washed away in the spin-coating process of the PMMA solution with chlorobenzene. To avoid the effects of moisture and oxygen, the glass/MAPbIBr/PCBM stacks were illuminated in the N_2-filled glovebox using the same LED light source as above. The changes in the (100) peak was identical to samples without PCBM. This observation shows that placing an electron transport layer does not suppress the halide migration. It is also consistent with many studies that implicate trapped holes as the cause of halide migration.[8,16–18]

We then examined glass/PTAA/MAPbIBr films (**Figure 1**g-l) under the same conditions and found that the phase segregation behavior was identical to glass/MAPbIBr films. For glass/MAPbIBr/PTAA, the changes in the (100) peak under illumination are similar to that of glass/PTAA/MAPbIBr whether the light enters from the top (PTAA side in this case) or bottom (glass/MAPbIBr side in this case) indicating that the direction of light dictates the vertical phase segregation pattern, regardless of the position of the PTAA HTL. (**Figure S2**a-f) We measured the full width at half maximum (FWHM) of (100) peaks with ω =3° before and after illumination aging and calculated the broadening ratio ($FWHM_{aged}/FWHM_{pristine}$) (**Table S1**). The peak broadening in powder X-ray diffraction has been correlated to halide phase

segregation.[25] We therefore used the FWHM broadening ratio as a qualitative measure of the phase segregation in the bulk. A ratio of ~1 indicates no change to the peak width whereas a ratio > 1 indicates broadening and thus phase segregation. After illumination, both glass/MAPbIBr and glass/PTAA/MAPbIBr showed increased FWHM broadening ratios. For these samples, we noticed that the illumination from the bottom led to a larger broadening ratio than from the top.

In the GIXRD measurements of glass/PTAA/CuI_xBr_{1-x}/MAPbIBr films, we noticed that the (100) diffraction peak of glass/PTAA/CuI/MAPbIBr did not noticeably change after illumination aging, indicating little or no halide segregation. When the light enters from the bottom, the (100) diffraction peaks with ω=0.5°, 1° and 3° remain stable, indicating both top and bottom interfaces and the bulk are resilient to phase segregation (**Figure 2**a-f). When light enters from the top, only a very slight shift was observed with ω=0.5°, which indicates a slight composition change at the top surface of MAPbIBr while the bulk of the MAPbIBr and the PTAA/CuI/MAPbIBr interface are stable. The vertical phase segregation is restricted to the vicinity of the top interface, away from the hole transport layers. The GIXRD pattern with glass/PTAA/$CuI_{0.5}Br_{0.5}$/MAPbIBr and glass/PTAA/CuBr/MAPbIBr are similar to glass/PTAA/CuI/MAPbIBr in which the phase segregation is also restricted to the vicinity of the top interface (**Figure S3**). The stability of the bulk of MAPbIBr on PTAA/CuI_xBr_{1-x} bilayers was confirmed by their FWHM broadening ratios. The stable (100) peaks suggest that PTAA/CuI_xBr_{1-x} is able to stabilize the HTL/MAPbIBr interface and MAPbIBr bulk.

For glass/MAPbIBr/CuI/PTAA films, the perovskite/HTL interface and bulk remain stable without signs of phase segregation (**Figure S2** g-l). For glass/MAPbIBr/$CuI_{0.5}Br_{0.5}$/PTAA and glass/MAPbIBr/CuBr/PTAA, when light is illuminated from the top (CuI_xBr_{1-x}/PTAA side in this case), the perovskite/HTL interface and bulk remain stable (**Figure S4** a-c and g-i). When the light is illuminated from the bottom (glass/MAPbIBr side in this case), the top perovskite/HTL interface is stable while a slight extent of composition change occurs close to the bottom interface, away from the CuI_xBr_{1-x}/PTAA hole transport bilayer (**Figure S4** d-f and j-l).

We then examined samples fabricated on ITO. In the ITO/MAPbIBr samples, the changes in the (100) peak were similar to glass/MAPbIBr and glass/PTAA/MAPbIBr (**Figure S5** a-f) but to a lesser extent, as indicated by the FWHM broadening ratio. For ITO/PTAA/MAPbIBr films also we observed changes in the (100) peak indicating phase segregation (**Figure S5** g-l).

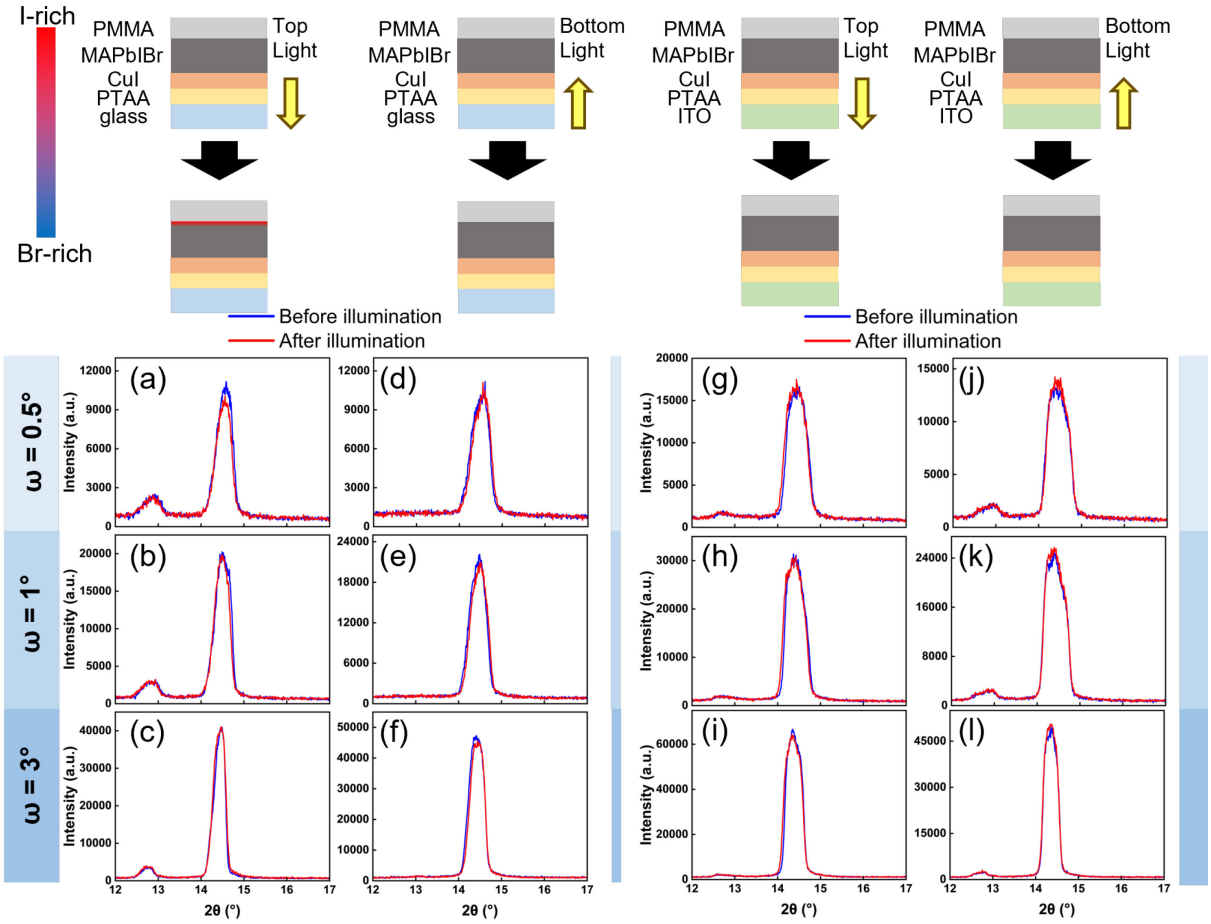

Figure 2. GIXRD patterns of (100) peak of (a-f) glass/PTAA/CuI/MAPbIBr and (g-l) ITO/PTAA/CuI/MAPbIBr with ω=0.5°, 1° and 3° before (blue) and after illumination (red). Schematic representations of light-induced vertical composition changes are attached to the top of each column of GIXRD patterns. For glass/PTAA/CuI/MAPbIBr, the light-induced phase segregation is limited to the top surface when light is from the top. For ITO/PTAA/CuI/MAPbIBr, the stable GIXRD pattern indicates suppression of phase segregation.

We, however, found that the phase segregation was effectively suppressed in ITO/PTAA/CuI_xBr_{1-x}/MAPbIBr. ITO/PTAA/CuI/MAPbIBr films show negligible change to the (100) peak (**Figure 2**g-l), while ITO/PTAA/$CuI_{0.5}Br_{0.5}$/MAPbIBr and ITO/PTAA/CuBr/MAPbIBr films show only minor (100) diffraction peak change near the top surface with light from top (**Figure S6**). MAPbIBr films with the PTAA/CuI_xBr_{1-x} bilayer on ITO exhibit FWHM broadening ratios closer to 1 than that on glass, indicating that ITO promotes the resilience of the MAPbIBr bulk against phase segregation. Overall, the GIXRD studies show that, under illumination, films with a hole transport bilayer had increased stability

and the most stable films had a hole transport bilayer on ITO substrates such as ITO/PTAA/CuI/MAPbIBr films.

To corroborate the GIXRD observations, we measured the changes in the bandgap after illumination aging using UV-visible absorption spectroscopy. As-prepared MAPbIBr films have a sharp absorption rise at 705 nm indicating the band edge. After illumination, the absorption spectra of glass/MAPbIBr and glass/PTAA/MAPbIBr exhibit a loss of absorption at 680 nm and the increased absorption in the 600 nm and 720 nm regions (**Figure 3**a and b), consistent with the loss of the mixed halide phase and the emergence of I^--rich and Br^--rich domains.[16,17] The absorption spectrum of ITO/MAPbIBr indicates a smaller degree of phase segregation. The absorption spectra of PTAA/CuI_xBr_{1-x}/MAPbIBr including those based on glass and ITO substrates, maintain most of their original sharp absorption characteristics after illumination (**Figure 3**a and b).

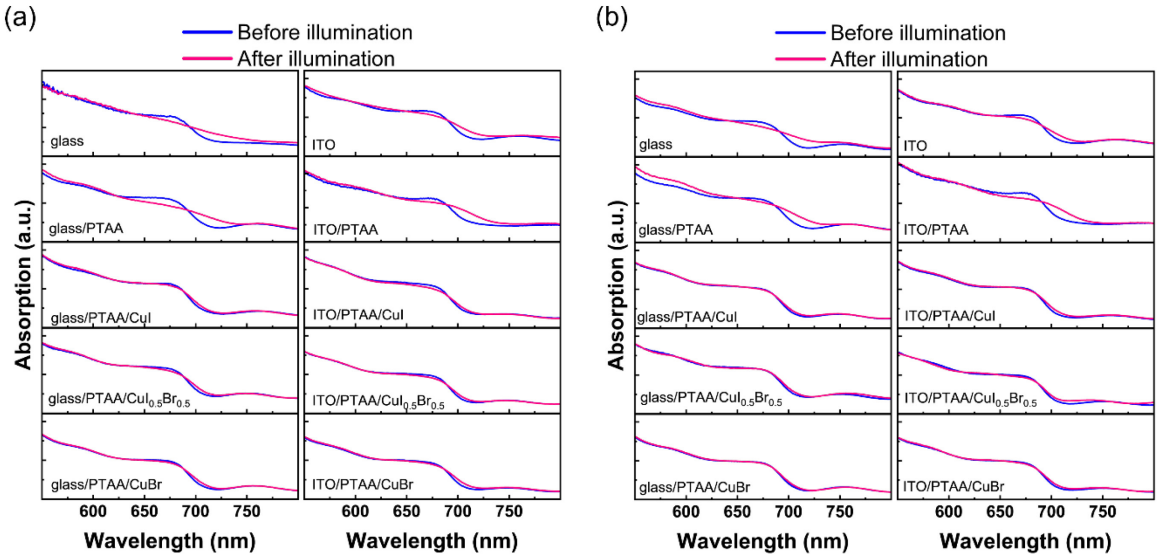

Figure 3. UV-vis absorption spectra of MAPbIBr films on glass substrates and with ITO coated-glass substrates with light entering from (a) top (MAPbIBr/PMMA side) and (b) bottom (substrate side). For glass, glass/PTAA, ITO and ITO/PTAA samples, the absorption spectra after illumination (pink) show a decrease at 680 nm and increase at 600 nm and 720 nm comparing the as-prepared samples (blue), indicating that the parent mixed phase segregates into I-rich and Br-rich domains. On the contrary, the absorption spectra of PTAA/CuI_xBr_{1-x} samples remain the sharp absorption onset at 705 nm.

We calculated the changes in the bandgap of the perovskite using Tauc plots obtained from the absorption spectra taken before and after illumination aging (**Table S2**). The as-prepared MAPbIBr films deposited on different HTL and substrates have a similar bandgap around 1.76

eV, which is consistent with the composition of $MAPbI_{(0.7}Br_{0.3)3}$.[27] After illumination either from the top or the bottom side, MAPbIBr films show different levels of bandgap reduction due to phase segregation and the trend is consistent with the observation from GIXRD. Overall, the samples with hole transport bilayers show minimum changes in the bandgap. ITO/PTAA/CuI_xBr_{1-x} samples, when illuminated from the ITO side, showed the least change (3 meV) whereas the MAPbIBr on a glass substrate showed the most change (100 meV). Moreover, ITO/PTAA/CuI_xBr_{1-x} (~3 to 8 meV) had a smaller change in bandgap than glass/PTAA/CuI_xBr_{1-x} (~9 to 15 meV) indicating the importance of the choice of substrates (conducting vs. insulating) and the importance of charge extraction. To quantify electronic disorder and thus the passivation effects of the HTL at the HTL/MAPbIBr interface, we computed Urbach energies (E_u) from the UV-vis absorption spectra of the MAPbIBr films before and after illumination aging (**Table S3**). Urbach energy can be regarded as a measure of disorder, including energetic disorder and disorder of the crystal lattice.[28,29] It is widely used to estimate the defect density and effect of passivation in perovskite materials.[30] We found that samples with perovskite deposited on PTAA/CuI_xBr_{1-x} bilayers have lower E_u (~52.6 to 53.5 meV) compared to samples with perovskite on PTAA or bare substrates (~77.8 to 85.8 meV). For all the samples, E_u increases after illumination. We found ITO/PTAA/$CuI_{0.5}Br_{0.5}$/MAPbIBr had the least increase in E_u (4.9 meV) and glass/MAPbIBr had the most increase (142.6 meV). We also observed that ITO/PTAA/CuI_xBr_{1-x}/MAPbIBr had a lower change in E_u (4.9 to 12.0 meV) compared to glass/PTAA/CuI_xBr_{1-x}/MAPbIBr (11.8 to 18.5 meV).

To characterize the charge extraction capabilities of different HTL, we performed steady-state photoluminescence spectroscopy (PL) on glass/HTL/MAPbIBr and ITO/HTL/MAPbIBr stacks. **Figure 4**a displays the PL spectra for glass-based stacks with different HTL configurations. Perovskite films on PTAA/CuI_xBr_{1-x} show better quenching than those on PTAA alone or on bare glass, implying better hole extraction by PTAA/CuI_xBr_{1-x} bilayers.[31] **Figure 4**b presents the corresponding PL spectra for ITO-based stacks. MAPbIBr on ITO exhibits the lowest PL intensity and PTAA/CuI_xBr_{1-x} bilayers on ITO also exhibit better quenching than PTAA on ITO alone. Comparing the same HTL on ITO and glass, we find that ITO leads to lower PL intensity, suggesting that ITO further facilitates hole extraction.

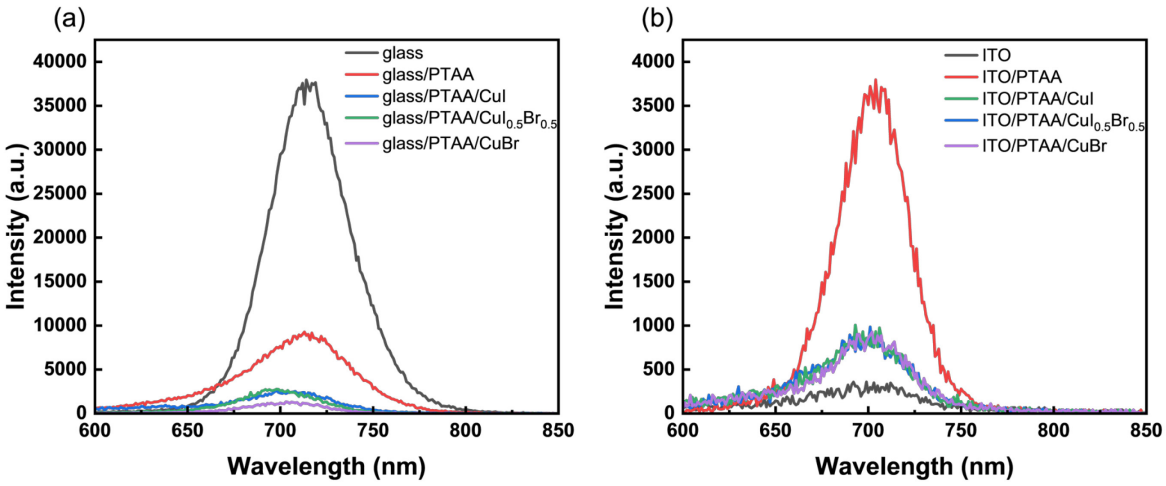

Figure 4. (a) Steady-state photoluminescence spectra of MAPbIBr films on glass substrates with different HTL. The intensities of PL from MAPbIBr films on HTL are low compared to MAPbIBr films on bare glass. This is likely due to hole extraction by the HTL and reducing charge recombination. (b) Steady-state photoluminescence spectra of MAPbIBr films on ITO-coated glass substrates with different HTLs. PTAA/CuI_xBr_{1-x} samples show lower PL intensity than samples on PTAA. All samples were excited by a 465 nm light from a Xeon lamp equipped with a monochromator.

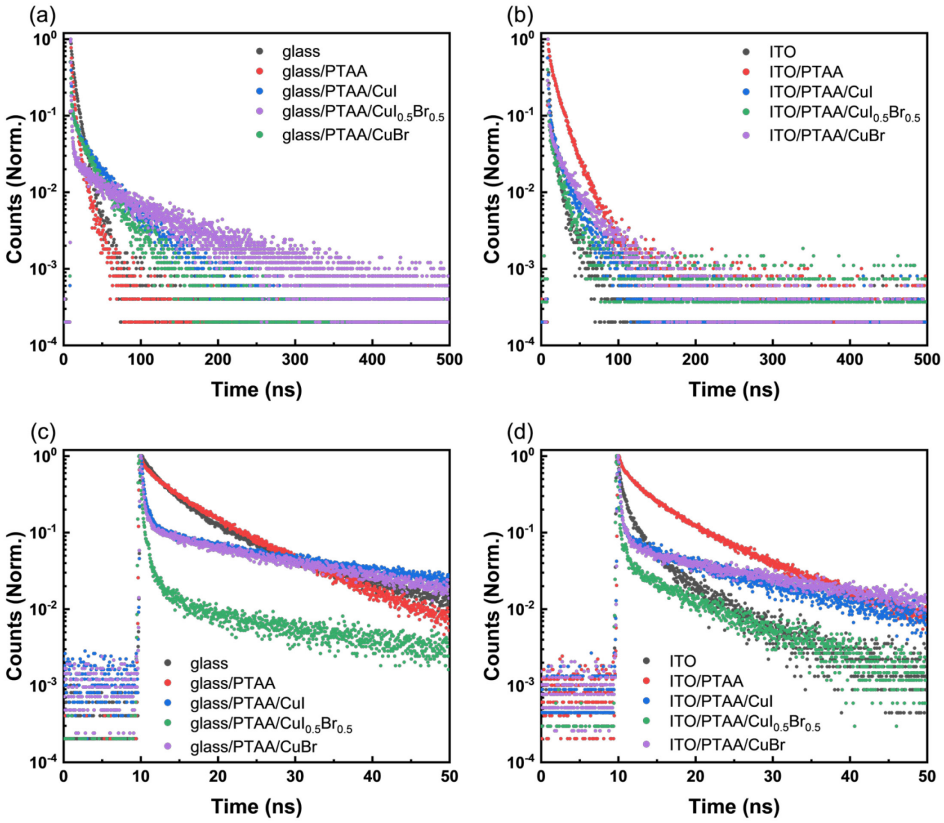

Figure 5. PL decay transients in the 500 ns range of MAPbIBr films on (a) glass substrates and (b) ITO-coated glass substrates. For both glass and ITO-coated glass substrates, PTAA/CuI_xBr_{1-x} samples exhibit faster PL decay than PTAA alone. It is noticed that the PL counts for PTAA/CuI_xBr_{1-x} samples drop quickly in the initial 50 ns. PL decay transient in the 50 ns range of MAPbIBr films on (c) glass substrates and (d) ITO-coated glass substrates show a clear biexponential decay profile for PTAA/CuI_xBr_{1-x} samples allowing deconvolution of hole extraction and non-radiative recombination processes.

We used time-resolved photoluminescence spectroscopy (TRPL) to understand the charge carrier dynamics in the HTL/MAPbIBr stacks. **Figure 5**a and b illustrate that MAPbIBr deposited on an HTL displays faster luminescence decay than on a bare glass substrate, resulting from the hole extraction by the HTL. The PL transients of all HTL/MAPbIBr exhibit a biexponential decay behavior. The decay of TRPL is governed by bimolecular radiative recombination, monomolecular, trap-assisted bulk or surface recombination, and charge transfer to HTL.[32–35] The TRPL decay in PTAA/CuI_xBr_{1-x}/MAPbIBr is notably quicker than in PTAA/MAPbIBr during the initial measurement period, which could potentially suggest a faster hole extraction. Additional TRPL measurements were conducted over a 50 ns range to further analyze the fast PL decay (shown in **Figure 5**c and d). Within this timeframe, the PTAA/CuI_xBr_{1-x} samples exhibit a distinct two-stage decay process. There is an initial rapid decay within approximately 5 ns followed by a slower single exponential decay. The clear 2-stage process allows us to distinguish the charge extraction and non-radiative recombination processes.[36] The fast PL counts decay is attributed to hole extraction while the single exponential decay is the characteristic of Shockley-Read-Hall recombination, which is attributed to interfacial recombination. In contrast, samples with only a single PTAA layer show indistinguishable charge extraction and interface recombination, likely due to elevated non-radiative recombination or suboptimal hole extraction.

Table 1. Summary of lifetime constants from fitting the PL transients of MAPbIBr films to the biexponential decay model.

Sample	τ_1(ns)	τ_2(ns)
glass	2.64	12.90
glass/PTAA	1.75	8.89
glass/PTAA/CuI	0.34	24.10
glass/PTAA/$CuI_{0.5}Br_{0.5}$	0.23	17.80
glass/PTAA/CuBr	0.23	21.03
ITO	0.54	5.02
ITO/PTAA	1.73	9.32

ITO/PTAA/CuI	0.14	14.90
ITO/PTAA/$CuI_{0.5}Br_{0.5}$	0.23	25.83
ITO/PTAA/CuBr	0.18	21.50

The PL transients within the 50 ns range were fitted using a biexponential decay model to compute the lifetime constants. As shown in **Table 1**, the shorter lifetimes τ_1 of PTAA/CuI_xBr_{1-x}-based MAPbIBr films are significantly smaller than the τ_1 of PTAA-based films, indicating a faster hole extraction. The longer lifetime τ_2 of PTAA/CuI_xBr_{1-x}/MAPbIBr is larger than the τ_2 of PTAA/MAPbIBr, indicating suppressed interface recombination, presumably due to interface passivation by CuI_xBr_{1-x}.

The biexponential fits of the PL transients are used to compute the differential lifetime (**Equation 1**), which is the inverse negative derivative of the logarithm of PL photon flux($\Phi(t)$). The differential lifetime representation allows us to separate the reduction of PL counts by different processes so that we can study the hole extraction in more detail.[2,37,38] The rise of τ_d at early times represents the charge extraction process (**Figure 6**a). The transition from rising to a plateau represents the end of the charge extraction process, and non-radiative recombination starts to take over. The steepness of the rising τ_d curve implies the speed of charge extraction. For PTAA/CuI_xBr_{1-x}, the τ_d curves exhibit a sharp rise with the saturation starting after ~3 ns, while the τ_d for PTAA exhibit a slower rise with the saturation starting after ~13 ns. This observation implies that the hole transfer to PTAA/CuI_xBr_{1-x} is faster than the hole transfer to PTAA.

$$\tau_d = -\{\frac{\mathrm{d}\ln[\Phi(t)]}{\mathrm{d}t}\}^{-1} \qquad (1)$$

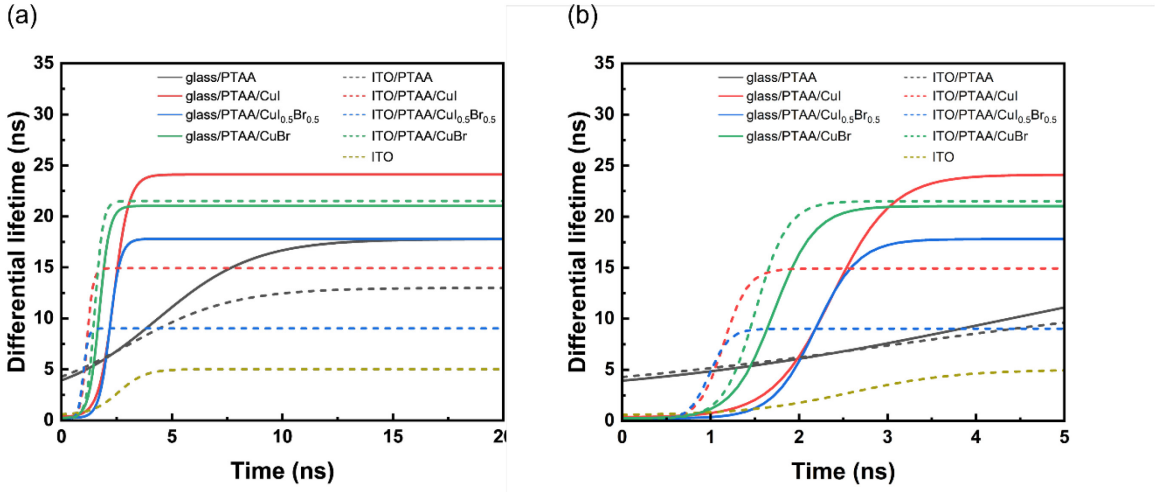

Figure 6. (a) Differential lifetime (τ_d) of MAPbIBr films computed by the biexponential fits of the PL transients. The rise at early times is determined by the speed of charge extraction. PTAA/CuI_xBr_{1-x} bilayers exhibit faster rise and saturation than PTAA alone, indicating faster

charge extraction. (b) The magnified differential lifetime plot within the range of 5 ns. Comparing the τ_d of MAPbIBr films with the same HTL on glass substrates (solid line) and on ITO-coated glass substrates (dash line), samples with ITO-coated glass as substrates (~1.2 to 2.1 ns) saturate faster than that with glass as substrates (~2.8 to 3.5 ns).

To study the impact of ITO on hole extraction, we compare the τ_d difference between glass and ITO-coated glass as substrates. For PTAA samples, there is no significant difference in τ_d with and without ITO. On the contrary, for PTAA/CuI_xBr_{1-x} samples, ITO accelerates the saturation of τ_d (**Figure 6**b), implying faster hole extraction. We surmise that the ITO helps to reduce the charge accumulation at the HTL/MAPbIBr interface by promoting efficient charge removal from the hole transport layers, particularly when the HTL itself efficiently facilitates charge extraction at this interface.

Krogmeier et al.[38] used numerical simulations to show that the shape of τ_d curve is affected by charge accumulation at the perovskite/charge selective layer interface. The extracted holes accumulate in the HTL, repel further holes from the perovskite layer, and slow down charge extraction. Due to the high conductivities of PTAA/CuI_xBr_{1-x} compared to PTAA,[19,20,39] the holes in HTL can be further transferred to the ITO layer, reducing the hole accumulation in PTAA/CuI_xBr_{1-x} and facilitating hole extraction from perovskite. Considering that ITO better promotes the suppression of phase segregation, we reason that using highly conductive HTL deposited on ITO can transfer holes away from the perovskite/HTL interface and reduce the accumulation of holes in HTL, which can further suppress phase segregation.

The above steady state PL and TRPL analysis indicate that PTAA/CuI_xBr_{1-x} results in better charge extraction and suppressed interface recombination than PTAA. ITO reduces charge accumulation in the highly conductive HTL, facilitating charge extraction.

To understand the fast hole extraction capabilities of PTAA/CuI_xBr_{1-x}, we performed capacitance-voltage measurements on full devices with the structure of ITO/HTL/MAPbIBr/PCBM/C_{60}-N/Ag. Mott-Schottky analysis was carried out on the dependence of C^{-2} on the bias (**Figure 7**). We are aware of the impact of ion migration and electrode polarization on the shape of the Mott-Schottky plot.[20,40] Mott-Schottky analysis is valid only when the linear depletion layer capacitance is clearly identified.[41]

The linear regions of the C^{-2}-V curves were fitted by the Mott-Schottky equation (**Equation 2**) to compute the built-in potential (V_{bi}) which is determined by fitting the linear region.[42]

$$\frac{1}{C^2} = \frac{2}{A^2 q \varepsilon_0 \varepsilon N_B}\left(V - V_{bi} - \frac{2kT}{q}\right) \qquad (2)$$

In **Equation 2**, A is the active area, ε_0 is the vacuum permittivity, ε is the relative dielectric constant of the perovskite, q is the elementary charge, N_B is the doping density, V_{bi} is the built-in potential, k is Boltzmann's constant, and T is the absolute temperature.

The V_{bi} of PSCs with PTAA, PTAA/CuI, PTAA/$CuI_{0.5}Br_{0.5}$, and PTAA/CuBr are 0.88 V, 1.00 V, 1.01 V, and 1.01 V, respectively. The larger V_{bi} of PTAA/CuI_xBr_{1-x} contributes to the more efficient extraction of photogenerated holes.

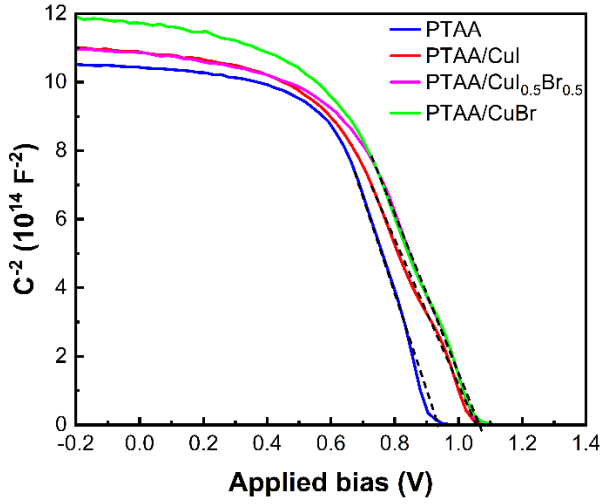

Figure 7. Mott-Schottky plot of PSCs fabricated based on PTAA and PTAA/CuI_xBr_{1-x} HTL. The *C-V* measurements were performed at 10 kHz with a scan rate of 120 mV s^{-1}.

The energy levels of the individual components in the HTL/MAPbIBr stacks were studied by ultraviolet photoelectron spectroscopy (UPS). **Figure 8**a shows the binding energy region for determining secondary cutoff energies (E_{SEC}). **Figure 8**b shows the binding energy region that displays valence band onsets. The work functions (WF) and valence band maximum (VBM) from these measurements are summarized in **Figure 8**c. The VBM of PTAA/CuI (-5.45 eV), PTAA/$CuI_{0.5}Br_{0.5}$ (-5.28 eV) and PTAA/CuBr (-5.38 eV) are closer to the VBM of MAPbIBr (-5.88 eV), than that of PTAA (-5.11 eV). The better VBM alignment of PTAA/CuI_xBr_{1-x} facilitates the hole extraction, which is corroborated by the TRPL measurements. Furthermore, the Fermi level of PTAA (-4.10 eV) is significantly shallower than that of MAPbIBr (-4.89 eV), generating an electric field at the interface that impedes hole extraction. This electric field opposes the built-in electric field in a p-i-n perovskite solar cell, diminishing the V_{bi}.[43] This is corroborated by the Mott-Schottky analysis. PTAA/CuI_xBr_{1-x}

exhibit deeper Fermi levels, which effectively mitigate the adverse electric field, optimizing the hole extraction.[44]

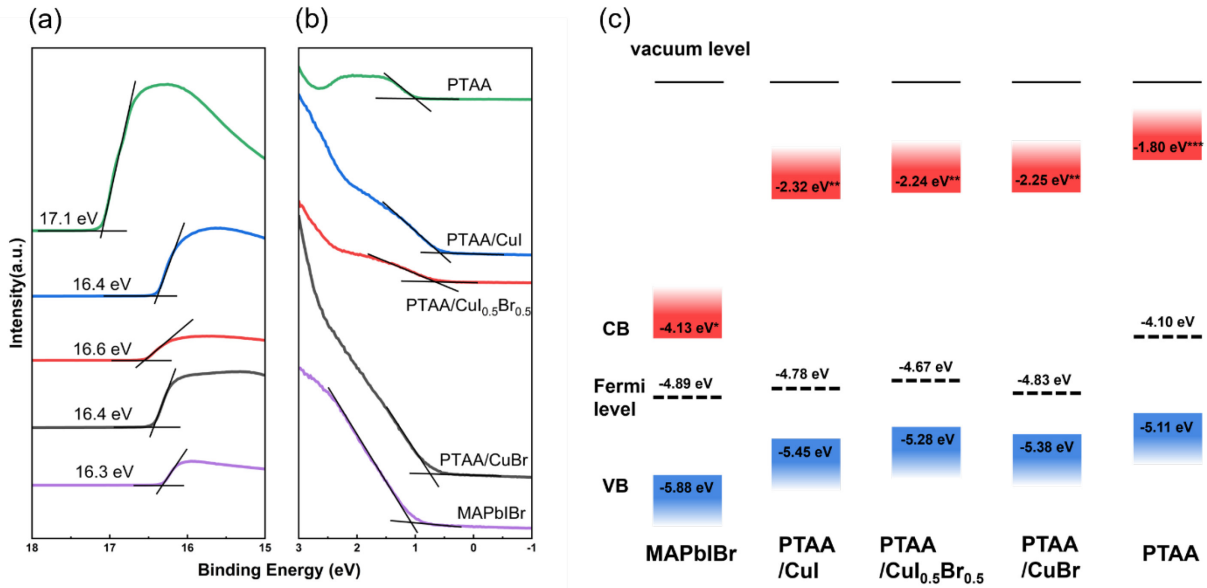

Figure 8. (a) Cutoff region and (b) VB edge region of UPS spectra of MAPbIBr, PTAA, PTAA/CuI, PTAA/$CuI_{0.5}Br_{0.5}$ and PTAA/CuBr on the ITO substrate. (c) Schematic illustration of the conduction band (CB), valence band (VB), and Fermi levels. *CB of MAPbIBr is calculated from the bandgap determined by absorption spectrum and VB determined by UPS. **CB of PTAA/CuI, PTAA/$CuI_{0.5}Br_{0.5}$ and PTAA/CuBr are calculated from the bandgap taken from reference 21. ***CB of PTAA is taken from reference 20.

Based on all our observations we are now able to address the question: what is the nature of the HTL that will lead to stable mixed halide devices? Comparing the stability of MAPbIBr on glass, bare ITO, glass/PTAA and glass/PTAA/CuI_xBr_{1-x} bilayers from GIXRD and UV-vis studies, we find that the degree of phase segregation is related to hole extraction. In **Figure S7**, we plot the bandgap reduction and FWHM broadening ratio vs. the PL peak intensity and PL lifetime to visualize the relationship between hole extraction and phase segregation. Glass and glass/PTAA samples have higher τ_1 and PL intensity, which indicate poorer charge extraction, and are associated with higher FWHM broadening ratio and bandgap reduction. Glass/PTAA/CuI_xBr_{1-x} samples with low τ_1 and PL intensity exhibit low FWHM broadening ratio and bandgap reduction while ITO with low τ_1 and PL intensity exhibit moderate FWHM broadening ratio and bandgap reduction.

When we compare HTL/MAPbIBr stacks on glass and ITO-coated glass substrates, the FWHM broadening ratio from GIXRD data and the bandgap changes from absorption data show that ITO-coated substrates suppress phase segregation in the presence of PTAA/CuI_xBr_{1-}

$_x$ bilayers. The differential lifetime plot (**Figure 6**b) from the TRPL study shows that ITO/PTAA/CuI_xBr_{1-x}/MAPbIBr samples have a shorter charge extraction saturation time than glass/PTAA/CuI_xBr_{1-x}/MAPbIBr samples, suggesting that ITO facilitates the hole extraction. We speculate that PTAA/CuI_xBr_{1-x} can efficiently transfer the extracted holes to the underlying ITO layer, which minimizes hole accumulation at the HTL/MAPbIBr interface. Thus, our findings suggest that the phase stability of MAPbIBr is improved by a combination of the efficient hole extraction from the perovskite layer to the HTL and the subsequent effective conduction of these holes to the electrode. Besides hole extraction, preventing hole accumulation at the HTL/MAPbIBr interface is crucial in further mitigating phase segregation.

When we compare ITO/MAPbIBr and ITO/PTAA/CuI_xBr_{1-x}/MAPbIBr, we observe that the phase segregation in ITO/MAPbIBr is lower than in glass/MAPbIbr but considerably higher than ITO/PTAA/CuI_xBr_{1-x}/MAPbIBr, even though ITO/MAPbIBr has comparable τ_1 and PL intensity to ITO/PTAA/CuI_xBr_{1-x}/MAPbIBr. The alleviation of phase segregation could be resulting from the high conductivity of ITO and the resultant efficient charge carrier extraction capability. The UV-vis study shows that PTAA/CuI_xBr_{1-x}/MAPbIBr have lower E_u (52.6 to 53.5 meV) due to passivation while ITO/MAPbIBr has a high E_u of 85.8 meV. The mere efficient extraction of photogenerated charge carriers by ITO is insufficient to prevent the phase segregation possibly because of the lack of passivation at the ITO/MAPbIBr interface, which is consistent with prior reports.[2]. After light aging, the E_u of glass/MAPbIBr, PTAA/MAPbIBr, and ITO/MAPbIBr significantly increase while the E_u of PTAA/CuI_xBr_{1-x}/MAPbIBr increases slightly. The increasing trend of the E_u of the MAPbIBr films is generally consistent with the decreasing trend of their bandgaps (i.e., the more the bandgap decreases, the more E_u increases). We attribute the increased defect density induced by ion migration. Thus, the low E_u after aging suggests that the passivated PTAA/CuI_xBr_{1-x}/MAPbIBr interface remains stable from detrimental ion migration under illumination. On the contrary, for ITO/MAPbIBr and PTAA/MAPbIBr, phase segregation is associated with a degraded perovskite/HTL interface. We conclude that a passivated and stable perovskite/HTL interface ensures long-term, stable, and efficient hole extraction, which is important to suppress phase segregation.

In a recent study, Suchan et al. proposed a two-stage model for phase segregation of mixed halide perovskites under illumination.[25] In stage 1, the photogenerated charge carriers rapidly concentrate in small domains to create high charge carrier densities and initiate phase segregation in its vicinity. Then, in stage 2, the localized high charge carrier densities create additional vacancies, which increases ionic mobility. This model is based on experimental results from a series of $MAPbI_xBr_{1-x}$ without any charge transport layers and the model does

not specify the nature of the charge carriers. The model also assumes that the charge density buildup is in the perovskite layer. Based on this model, we expect that adding charge transport layers will prevent the buildup of charge-carrier density in the perovskite layer in stage 1 through hole extraction and thus suppress phase segregation. If the charges are continuously extracted, then the creation of additional vacancies in stage 2 is also prevented. Then why does extracting the charges from the active layer by the charge transport layer alone not seem to arrest the halide migration?

We believe that our results provide some of the missing pieces. Based on our observation that the samples with and without PCBM behaved similarly, we conclude that the accumulation of the holes is the origin of halide phase segregation. Our work also shows that extracting holes from the bulk of MAPbIBr to the HTL can alleviate phase segregation to some extent. More importantly, we find that transferring the extracted holes away from the MAPbIBr/HTL interface to the underlying ITO electrode is key to further suppressing the phase segregation. Our observations show that any accumulation of holes at the MAPbIBr/HTL interface may also trigger processes in stage 1 and stage 2 identified by Suchan et al. We also find that passivating the HTL/MAPbIBr interface by CuI_xBr_{1-x} makes MAPbIBr resilient to photo-induced defect generation and facilitates suppression of phase segregation compared to mere hole extraction.

Overall, our work showcases a strategy of interface engineering that reduces the hole localization in stage 1 and defect accumulation in stage 2. Based on our results, we propose that there is a dynamic vicious cycle between photogenerated hole accumulation, defect generation, ion migration and vertical phase segregation. (**Figure S8**) The pre-existing defects at the perovskite/HTL interface and photogenerated holes accelerate the ion migration which leads to the destruction of the crystal lattice and the formation of more defects. The defects generated in this process in turn accelerate defect-mediated ion migration and deteriorate the integrity of the HTL/MAPbIBr interface. The degraded MAPbIBr/HTL interface reduces hole extraction efficiency, thus causing more severe hole accumulation. Overall, the accumulation of defects and photogenerated holes becomes increasingly severe through this vicious cycle, resulting in directional ion migration and phase segregation.

We propose that an HTL with synergetic passivation, efficient hole extraction and transport of holes away from the perovskite/HTL interface are vital to arrest the phase segregation. The efficient hole extraction by the PTAA/CuI_xBr_{1-x} bilayer reduces photogenerated hole density and gradient, weakening the driving force of directional halide redistribution. The high conductivity of the PTAA/CuI_xBr_{1-x} contributes to reducing the hole accumulation by transferring the holes to the ITO electrode, which facilitates hole extraction from MAPbIBr. In

addition, the interfacial passivation suppresses the ion migration at the interface where phase segregation begins, maintaining a stable MAPbIBr/HTL interface to efficiently extract holes. The PTAA/CuI_xBr_{1-x} bilayer comprehensively suppresses the driving forces and pathways for vertical phase segregation, improving the photostability of mixed-halide perovskite.

3. Conclusion

In summary, we have comprehensively investigated the impact of HTL on light-induced vertical phase segregation of mixed-halide perovskite. We employed GIXRD and UV-vis absorption spectroscopy to monitor the light-induced vertical phase segregation of MAPbIBr films deposited on different HTL and substrates. GIXRD analysis reveals that vertical phase segregation occurs to MAPbIBr deposited on glass, ITO and PTAA. The ion migration direction is dictated by the incident light direction. Specifically, iodide-rich regions are located near the illuminated surface, while bromide-rich regions are located further away from the illuminated surface. Vertical phase segregation is significantly suppressed in MAPbIBr films on the PTAA/CuI_xBr_{1-x} bilayer HTL. We also found that depositing PTAA/CuI_xBr_{1-x}/MAPbIBr on ITO-coated glass as substrates can further suppress phase segregation, stressing the importance of having the holes staying away from the MAPbIBr layer for better stability.

Next, we measured photoluminescence and capacitance-voltage curves (Mott-Schottky analysis) to investigate the electronic properties of HTL to understand their link to phase segregation. Steady-state and time-resolved PL indicate superior efficiency of the PTAA/CuI_xBr_{1-x} bilayer HTL in extracting photogenerated holes from the MAPbIBr layer compared to the single-layer PTAA HTL. Mott-Schottky analysis reveals that PSCs based on PTAA/CuI_xBr_{1-x} HTL possess larger built-in electric fields, providing improved driving force for charge extraction. Furthermore, MAPbIBr films on PTAA/CuI_xBr_{1-x} exhibit lower Urbach energies than those on PTAA, glass, or ITO, underscoring the effective passivation capabilities of the PTAA/CuI_xBr_{1-x} bilayer. Thus, our findings suggest that the synergetic interplay of passivation, efficient hole extraction and the transport of holes away from the perovskite/HTL interface packs a more powerful punch for suppressing the light-induced vertical phase segregation in mixed-halide perovskite. In the design of HTL for stable mixed-halide perovskite optoelectronic devices, comprehensive considerations of efficient photogenerated hole extraction and interface passivation capability are key to stable and efficient PSCs. This comprehensive understanding paves the way for the development of light-stable optoelectronic devices based on mixed-halide perovskite, which is a critical step forward in the advancement of perovskite LEDs and perovskite tandem cells.

4. Experimental Section

Materials: The indium tin oxide (ITO)-coated glass substrates were from Kintec Company. PTAA, CuI, CuBr, PMMA were purchased from Sigma-Aldrich. PbI_2 is from Thermo Fisher. Methylammonium iodide (MAI) and methylammonium bromide (MABr) were purchased from Greatcell Solar Materials. PCBM was purchased from Nano-C. C60-N was purchased from 1-Material. Dimethyl sulfoxide (DMSO), gamma-butyrolactone (GBL), acetonitrile, chlorobenzene (CB), trifluoroethanol (TFE), and isopropyl alcohol (IPA) were purchased from Alfa Aesar.

Fabrication of MAPbIBr films: Glass and ITO-coated glass substrates were ultrasonicated in soap water, water, acetone, and isopropyl alcohol for 10 min, respectively. PTAA solution was prepared by dissolving PTAA in chlorobenzene (1.5 mg mL^{-1}). CuI and CuBr solutions were prepared by dissolving CuI (15 mg mL^{-1}) or CuBr (11.3 mg mL^{-1}) in acetonitrile. $CuI_{0.5}Br_{0.5}$ solution was prepared by mixing CuI and CuBr solutions (volume ratio 1:1). The $MAPb(I_{0.7}Br_{0.3})_3$ precursor solution (1.4 M) was prepared by dissolving MAI (22.2 mg), MABr (148.1 mg), and PbI_2 (645.5 mg) in GBL:DMSO (v:v 7:3). The $MAPb(I_{0.7}Br_{0.3})_3$ precursor solution was stirred at 60 °C overnight. PMMA solution (150 mg mL^{-1}) was prepared by dissolving PMMA in chlorobenzene and being stirred overnight at 60 °C.

The PTAA solution was spin-coated on glass or ITO-coated glass substrates at 4000 rpm for 30 s, followed by annealing at 100°C for 10 min. For PTAA/CuI_xBr_{1-x} bilayers, CuI_xBr_{1-x} solutions were spin-coated on the PTAA layer at 3000 rpm for 60 s, followed by annealing at 100 °C for 10 min. $MAPb(I_{0.7}Br_{0.3})_3$ precursor solution was spin-coated on the PTAA or PTAA/CuI_xBr_{1-x} bilayer by a two-step procedure(1500 rpm for 20s followed by 2000 rpm for 60 s).[20] During the second step, 200 uL of chlorobenzene was dripped on the substrate after 20 s. The perovskite films were annealed at 100 °C for 10 min. In the last step, 50 uL of PMMA was spin-coated on the perovskite films at 2000 rpm to encapsulate the perovskite films. For glass/MAPbIBr/PCBM samples, PCBM solution was spin-coated on the MAPbIBr layer at 2000 rpm for 60 s and no PMMA was deposited on top as the encapsulation layer to avoid washing away the PCBM layer.

Fabrication of PSCs: For the fabrication of PSCs for electrical measurements, the precursor preparation and coating procedures were the same as those in the fabrication of MAPbIBr films without PMMA encapsulation. For the electron transport layer, PCBM (20 mg mL^{-1} in chlorobenzene) was spin-coated on the perovskite films at 2000 rpm for 30 s. Then, C60-N (3 mg mL^{-1} in trifluoroethanol) was spin-coated on PCBM at 4000 rpm for 30 s. Finally, silver was deposited on C60-N by thermal evaporation to form a 100 nm-thick electrode.

Grazing Incidence X-ray Diffraction (GIXRD): GIXRD measurements were performed by a Rigaku SmartLab SE X-ray diffractometer with a Cu Kα source (1.542 Å). The height of the thin film samples was calibrated before each scanning. The incident angle (ω) of the X-ray was set to be 0.5°, 1°, and 3°, respectively. The samples were scanned in the 2θ range of 10° to 40°.

UV-vis Absorption Spectroscopy: The UV-vis absorption spectrum was obtained by a Shimadzu UV-2401 PC spectrophotometer where the scanning range is 550-900 nm.

Steady-state and time-resolved photoluminescence measurements (TRPL): The steady-state PL was obtained by a Horiba Fluorolog-3 spectrometer. The samples were excited by the 465 nm light from a Xeon lamp with a monochromator. The emission spectrum was collected ranging from 550 to 900 nm. The TRPL was obtained by an Edinburgh FLS1000 Fluorometer using a 400 nm laser (EPL-405, pulse width ~55 ps) as the excitation source. The emission lifetimes were determined by reconvolution fits using the experimentally measured instrument function (IRF).

Mott-Schottky Analysis (MS): The C-V measurements for Mott-Schottky analysis were obtained by a Solartron Analytical Electrochemical Impedance Analyzer with an SI 1287 electrochemical interface and a 1252 A frequency response analyzer. The capacitance-bias data was collected by sweeping voltage from -0.2 to 1.2 V at 10 kHz frequency with 50 mV of AC amplitude.

Ultraviolet Photoelectron Spectroscopy (UPS): The ultraviolet photoelectron spectra were acquired by a PHI 5600 XPS system with a third-party data acquisition system (RBD Instruments, Bend Oregon) at a base pressure of $<1 \times 10^{-9}$ Torr. Instrumental calibration included positioning XP spectral features for Cu $2p_{3/2}$ at 932.67 eV and Au $4f_{7/2}$ at 84.00 eV on freshly sputter-cleaned samples that yielded Fermi-level positioning for a UP spectral assignment of $E_{F,Au} \equiv 0.00 \pm 0.050$ eV. A He discharge lamp (PREVAC, Rogów, Poland) was used as the UV excitation source ($\mathbf{E}_{\mathrm{He\ I}} = h\nu = 21.218$ eV) and a hemispherical energy analyzer was used to collect the photoelectrons and the sample stage was positioned for a collection angle of 0° with respect to the sample normal angle. A –35 V bias vs the electrically grounded chamber assured linearity in the UV photoelectron transmission to the analyzer based on spectrum invariance for biases between –20 and –50 V. Acquisition conditions utilized a hemispherical pass energy of 5.85 V, a step size of 25 meV, and 50 ms acquisition times per step.

Supporting Information

Supporting Information is available from the Wiley Online Library or from the author.

Acknowledgements

DV and ZZ acknowledge support from US National Science Foundation (NSF) DMR 2101127. We also thank PPG Foundation for a graduate fellowship to ZZ. The powder X-ray diffractometer, which was used for our studies, was purchased through NSF Major Research Instrumentation grant CHE-1726578. RJG acknowledges funding support from NSF CMMI-2223664. TM acknowledges NSF under Grant CHE-2144787, an NSF CAREER Award.

Received: ((will be filled in by the editorial staff))

Revised: ((will be filled in by the editorial staff))

Published online: ((will be filled in by the editorial staff))

References

[1] E. T. Hoke, D. J. Slotcavage, E. R. Dohner, A. R. Bowring, H. I. Karunadasa, M. D. McGehee, *Chem Sci* **2015**, *6*, 613.
[2] A. Al-Ashouri, E. Köhnen, B. Li, A. Magomedov, H. Hempel, P. Caprioglio, J. A. Márquez, A. B. Morales Vilches, E. Kasparavicius, J. A. Smith, N. Phung, D. Menzel, M. Grischek, L. Kegelmann, D. Skroblin, C. Gollwitzer, T. Malinauskas, M. Jošt, G. Matič, B. Rech, R. Schlatmann, M. Topič, L. Korte, A. Abate, B. Stannowski, D. Neher, M. Stolterfoht, T. Unold, V. Getautis, S. Albrecht, *Science* **2020**, *370*, 1300.
[3] F. Xu, M. Zhang, Z. Li, X. Yang, R. Zhu, *Adv. Energy Mater.* **2023**, *13*, 2203911.
[4] M. C. Brennan, S. Draguta, P. V. Kamat, M. Kuno, *ACS Energy Lett.* **2018**, *3*, 204.
[5] C. G. Bischak, C. L. Hetherington, H. Wu, S. Aloni, D. F. Ogletree, D. T. Limmer, N. S. Ginsberg, *Nano Lett.* **2017**, *17*, 1028.
[6] D. Di Girolamo, N. Phung, F. U. Kosasih, F. Di Giacomo, F. Matteocci, J. A. Smith, M. A. Flatken, H. Köbler, S. H. Turren Cruz, A. Mattoni, L. Cinà, B. Rech, A. Latini, G. Divitini, C. Ducati, A. Di Carlo, D. Dini, A. Abate, *Adv. Energy Mater.* **2020**, *10*, 2000310.
[7] L. Hu, X. Guan, W. Chen, Y. Yao, T. Wan, C.-H. Lin, N. D. Pham, L. Yuan, X. Geng, F. Wang, C.-Y. Huang, J. Yuan, S. Cheong, R. D. Tilley, X. Wen, D. Chu, S. Huang, T. Wu, *ACS Energy Lett.* **2021**, *6*, 1649.
[8] G. F. Samu, Á. Balog, F. De Angelis, D. Meggiolaro, P. V. Kamat, C. Janáky, *J. Am. Chem. Soc.* **2019**, *141*, 10812.
[9] R. A. Kerner, Z. Xu, B. W. Larson, B. P. Rand, *Joule* **2021**, *5*, 2273.
[10] Z. Ni, H. Jiao, C. Fei, H. Gu, S. Xu, Z. Yu, G. Yang, Y. Deng, Q. Jiang, Y. Liu, Y. Yan, J. Huang, *Nat. Energy* **2022**, *7*, 65.
[11] Z. Xu, D. D. Astridge, R. A. Kerner, X. Zhong, J. Hu, J. Hong, J. A. Wisch, K. Zhu, J. J. Berry, A. Kahn, A. Sellinger, B. P. Rand, *J. Am. Chem. Soc.* **2023**, *145*, 11846.
[12] D. W. deQuilettes, W. Zhang, V. M. Burlakov, D. J. Graham, T. Leijtens, A. Osherov, V. Bulović, H. J. Snaith, D. S. Ginger, S. D. Stranks, *Nat. Commun.* **2016**, *7*, 11683.
[13] Alexander J. Knight, Adam D. Wright, Jay B. Patel, David P. McMeekin, Henry J. Snaith, Michael B. Johnston, Laura M. Herz, *ACS Energy Lett.* **2019**, *4*, 75.

[14] A. J. Barker, A. Sadhanala, F. Deschler, M. Gandini, S. P. Senanayak, P. M. Pearce, E. Mosconi, A. J. Pearson, Y. Wu, A. R. Srimath Kandada, T. Leijtens, F. De Angelis, S. E. Dutton, A. Petrozza, R. H. Friend, *ACS Energy Lett.* **2017**, *2*, 1416.
[15] C. G. Bischak, A. B. Wong, E. Lin, D. T. Limmer, P. Yang, N. S. Ginsberg, *J. Phys. Chem. Lett.* **2018**, *9*, 3998.
[16] J. T. DuBose, P. V. Kamat, *J. Am. Chem. Soc.* **2020**, *142*, 5362.
[17] J. T. DuBose, P. V. Kamat, *Acc. Mater. Res.* **2022**, *3*, 761.
[18] V. J.-Y. Lim, A. J. Knight, R. D. J. Oliver, H. J. Snaith, M. B. Johnston, L. M. Herz, *Adv. Funct. Mater.* **2022**, *32*, 2204825.
[19] H. Javaid, N. Heller, V. V. Duzhko, N. Hight-Huf, M. D. Barnes, D. Venkataraman, *ACS Appl. Energy Mater.* **2022**, *5*, 8075.
[20] H. Javaid, V. V. Duzhko, D. Venkataraman, *ACS Appl. Energy Mater.* **2021**, *4*, 72.
[21] N. Yamada, Y. Tanida, H. Murata, T. Kondo, S. Yoshida, *Adv. Funct. Mater.* **2020**, *30*, 2003096.
[22] C. Zhang, X. Shen, M. Chen, Y. Zhao, X. Lin, Z. Qin, Y. Wang, L. Han, *Adv. Energy Mater.* **2023**, *13*, 2203250.
[23] S. Chen, X. Xiao, B. Chen, L. L. Kelly, J. Zhao, Y. Lin, M. F. Toney, J. Huang, *Sci. Adv.* **2021**, *7*, eabb2412.
[24] R. G. Balakrishna, S. M. Kobosko, P. V. Kamat, *ACS Energy Lett.* **2018**, *3*, 2267.
[25] K. Suchan, J. Just, P. Beblo, C. Rehermann, A. Merdasa, R. Mainz, I. G. Scheblykin, E. Unger, *Adv. Funct. Mater.* **2023**, *33*, 2206047.
[26] E. Shirzadi, N. Tappy, F. Ansari, M. K. Nazeeruddin, A. Hagfeldt, P. J. Dyson, *Adv Sci Weinh* **2022**, e2103729.
[27] W. Zhu, C. Bao, F. Li, X. Zhou, J. Yang, T. Yu, Z. Zou, *Chem. Commun.* **2015**, *52*, 304.
[28] E. Ugur, M. Ledinský, T. G. Allen, J. Holovský, A. Vlk, S. De Wolf, *J. Phys. Chem. Lett.* **2022**, *13*, 7702.
[29] Y. Liu, J.-P. Banon, K. Frohna, Y.-H. Chiang, G. Tumen-Ulzii, S. D. Stranks, M. Filoche, R. H. Friend, *ACS Energy Lett.* **2023**, *8*, 250.
[30] S. Cacovich, D. Messou, A. Bercegol, S. Béchu, A. Yaiche, H. Shafique, J. Rousset, P. Schulz, M. Bouttemy, L. Lombez, *ACS Appl. Mater. Interfaces* **2020**, *12*, 34784.
[31] Z. Zhang, M. Sheri, Z. A. Page, T. Emrick, A. Saeki, Y. Liu, T. P. Russell, *ACS Appl. Mater. Interfaces* **2020**, *12*, 56068.
[32] Alexander J. Knight, Jay B. Patel, Henry J. Snaith, Michael B. Johnston, Laura M. Herz, *Adv. Energy Mater.* **2020**, *10*, 1903488.
[33] X. Lai, F. Meng, Q.-Q. Zhang, K. Wang, G. Li, Y. Wen, H. Ma, W. Li, X. Li, A. K. K. Kyaw, K. Wang, X. W. Sun, M. Du, X. Guo, J. Wang, W. Huang, *Sol. RRL* **2019**, *3*, 1900011.
[34] M. Stolterfoht, C. M. Wolff, J. A. Márquez, S. Zhang, C. J. Hages, D. Rothhardt, S. Albrecht, P. L. Burn, P. Meredith, T. Unold, D. Neher, *Nat. Energy* **2018**, *3*, 847.
[35] F. Qi, X. Deng, X. Wu, L. Huo, Y. Xiao, X. Lu, Z. Zhu, A. K.-Y. Jen, *Adv. Energy Mater.* **2019**, *9*, 1902600.
[36] Y. Yang, C. Liu, Y. Ding, Z. Arain, S. Wang, X. Liu, T. Hayat, A. Alsaedi, S. Dai, *ACS Appl. Mater. Interfaces* **2019**, *11*, 34964.
[37] L. Krückemeier, B. Krogmeier, Z. Liu, U. Rau, T. Kirchartz, *Adv. Energy Mater.* **2021**, *11*, 2003489.
[38] B. Krogmeier, F. Staub, D. Grabowski, U. Rau, T. Kirchartz, *Sustain. Energy Fuels* **2018**, *2*, 1027.
[39] S. Lee, H. J. Lee, Y. Ji, S. M. Choi, K. H. Lee, K. Hong, *J. Mater. Chem. C* **2020**, *8*, 9608.
[40] O. Almora, C. Aranda, G. Garcia-Belmonte, *J. Phys. Chem. C* **2018**, *122*, 13450.

[41] O. Almora, C. Aranda, E. Mas-Marzá, G. Garcia-Belmonte, *Appl. Phys. Lett.* **2016**, *109*, 173903.
[42] K. Gelderman, L. Lee, S. W. Donne, *J. Chem. Educ.* **2007**, *84*, 685.
[43] S. Wang, T. Sakurai, W. Wen, Y. Qi, *Adv. Mater. Interfaces* **2018**, *5*, 1800260.
[44] S. Tan, T. Huang, I. Yavuz, R. Wang, T. W. Yoon, M. Xu, Q. Xing, K. Park, D. K. Lee, C. H. Chen, R. Zheng, T. Yoon, Y. Zhao, H. C. Wang, D. Meng, J. Xue, Y. J. Song, X. Pan, N. G. Park, J. W. Lee, Y. Yang, *Nature* **2022**, *605*, 268.